PHYSICAL REVIEW B **90**, 075428 (2014)

# Spontaneous strains and gap in graphene on boron nitride

Pablo San-Jose, A. Gutiérrez-Rubio, Mauricio Sturla, and Francisco Guinea
*Instituto de Ciencia de Materiales de Madrid, Consejo Superior de Investigaciones Científicas,*
*Sor Juana Inés de la Cruz 3, 28049 Madrid, Spain*

(Received 2 June 2014; revised manuscript received 1 August 2014; published 25 August 2014)

The interaction between a graphene layer and a hexagonal boron nitride (hBN) substrate induces lateral displacements and strains in the graphene layer. The displacements lead to the appearance of commensurate regions and the existence of an average gap in the electronic spectrum of graphene. We present a simple, but realistic, model, with which the displacements, strains, and spectral gap can be derived analytically from the adhesion forces between hBN and graphene. When the lattice axes of graphene and the substrate are aligned, strains reach a value of the order of 2%, leading to effective magnetic fields above 100 T. The combination of strains and induced scalar potential gives a sizable contribution to the electronic gap. Commensuration effects are negligible due to the large stiffness of graphene.

DOI: 10.1103/PhysRevB.90.075428 PACS number(s): 62.20.F−, 73.22.Pr, 42.30.Ms

## I. INTRODUCTION

Hexagonal boron nitride (hBN) has been demonstrated as a promising insulating substrate for graphene. Both systems share the same lattice structure, with a lattice mismatch of $\delta = 1.8\%$. hBN is an insulator with an ~5.2-eV gap. The electronic carriers in graphene on hBN exhibit very large mobilities [1–5].

The electronic band structure of graphene placed over hBN is being intensively studied, both theoretically [6–16] and experimentally [17–21]. The earliest experiments on different samples showed conflicting results regarding the existence of an insulating state at the neutrality point. Some experiments [22,23] suggested the existence of an electronic gap of about ~30 meV [22], while others did not see any clear evidence of it [2,3]. There is a growing consensus that inhomogeneous strains in the graphene layer may be the underlying mechanism for gap opening [14]. While an unstrained and flat graphene monolayer on hBN is expected to be gapless, corrugations and in-plane strains should open a spectral gap. The effects of corrugations was recently studied in Ref. [24].

A recent experiment [21] strongly suggests the existence of a correlation between the electronic gap and the formation of a peculiar in-plane strain pattern on graphene, measured both through conductive atomic force microscopy (AFM) and through scanning tunnel microscopy (STM). In the absence of strains (i.e., at large enough rotation angles between the lattice axes, $\theta \gtrsim 1^\circ$), both imaging techniques yield a smoothly varying signal across the sample, following the moiré pattern corresponding to the mismatch $\delta$ and the angle $\theta$. As $\theta$ is decreased below $1^\circ$, however, a sudden jump in the AFM and STM patterns occurs. The new AFM pattern is composed of uniform commensurate hexagonal regions, surrounded by sharp boundaries. It is argued that the hBN crystal creates a rapidly varying adhesion potential landscape [7,13] to which graphene tries to adapt by deforming. At low angles, within the commensurate hexagonal regions, graphene is strained to locally compensate for the small rotation and lattice mismatch, thus becoming in registry with the hBN crystal. The accumulated strain is released at the sharp hexagon boundaries. The locally averaged lattice constant, related to the trace of the strain tensor, is measured directly by STM and is found to differ between hexagonal regions and their boundaries by around 2%.

We present here a description of the strains in graphene induced by its adhesion to hBN. We provide an analytical solution for the strains as a function of the twist angle. Using known elastic constants for graphene and first-principles results for the adhesion potential, we compute the graphene distortion field that globally minimizes the sum of the elastic energy and the adhesion energy. We obtain maximum values for the local expansion of graphene in agreement with the experiment in Ref. [21]. We also find associated pseudomagnetic fields exceeding 200 T that are, however, nonmonotonous in the twist angle and exhibit a global field inversion at a particular angle around 1.5°. We furthermore characterize the adhesion energy density of the equilibrium graphene solution and find spatial patterns similar to those in the experiment, with uniform hexagonal regions surrounded by sharp boundaries. Our description of this system provides a simple analytical and quantitative description of most of the features in Ref. [21]. It may also be used as the basis for an electronic structure computation, particularly for evaluating the electronic spectral gap associated with these deformations.

This paper is organized as follows. In Sec. II, we set our notation and characterize the geometric moiré pattern as a function of lattice mismatch and twist angle. In Sec. III we describe our model for the energetics of adhesion and strain and write the equilibrium solution for the displacements. We also obtain expressions for the associated pseudomagnetic field. In Sec. IV we plot and discuss the results, including the spectral gap caused by the deformations in Sec. V. Finally, we draw our conclusions in Sec. VI.

## II. MOIRÉ SUPERLATTICE

Graphene and hBN exhibit a $\delta \approx 1.8\%$ lattice mismatch, $a'_0 = (1+\delta)a_0$, where $a_0 = 0.246$ nm and $a'_0 = 0.251$ nm are the lattice parameters of graphene and hBN, respectively. Thus, a graphene monolayer placed on an hBN crystal will not be in perfect registry, even if their crystallographic axes are perfectly aligned. If both crystals remain strain free when brought into contact, this results in the formation of a smooth hexagonal moiré pattern with period $A_0 \approx 14$ nm. If the two crystals are rotated by a relative angle $\theta$, the moiré period is reduced. The general form of $A_0$ is

$$A_0 = |\vec{A}_1| = |\vec{A}_2| = \frac{1+\delta}{\sqrt{1+(1+\delta)^2-2(1+\delta)\cos\theta}}a_0, \tag{1}$$

where $\vec{A}_i$ are the superlattice vectors and $|\theta| \leqslant 30^\circ$. This result, and also general expressions for $\vec{A}_i$, is derived as follows. We write $\vec{A}_i$ and the corresponding graphene and hBN lattice vectors $\vec{a}_i$ and $\vec{a}_i'$ as the columns of the $2\times 2$ matrices $\boldsymbol{A} = (\vec{A}_1,\vec{A}_2) = \boldsymbol{G}^{-1}/2\pi$, $\boldsymbol{a} = (\vec{a}_1,\vec{a}_2) = \boldsymbol{g}^{-1}/2\pi$, and $\boldsymbol{a}' = (\vec{a}_1',\vec{a}_2') = \boldsymbol{g}'^{-1}/2\pi$. By defining the mismatch-plus-rotation transformation $\boldsymbol{a}' = \boldsymbol{R}\boldsymbol{a}$ between the two lattices,

$$\boldsymbol{R} = (1+\delta)\begin{pmatrix}\cos\theta & -\sin\theta\\ \sin\theta & \cos\theta\end{pmatrix}, \tag{2}$$

and by noting that the conjugate momenta of the moiré pattern (rows of matrix $\boldsymbol{G}$) are defined as the mismatch between lattice momenta $\boldsymbol{G} = \boldsymbol{g} - \boldsymbol{g}'$ [25], we find $\boldsymbol{A} = \boldsymbol{a}\boldsymbol{N} = \boldsymbol{a}'\boldsymbol{N}'$, where $\boldsymbol{N} = \boldsymbol{a}^{-1}(\mathbb{1}-\boldsymbol{R}^{-1})^{-1}\boldsymbol{a}$ and $\boldsymbol{N}' = \boldsymbol{a}^{-1}(\boldsymbol{R}-\mathbb{1})^{-1}\boldsymbol{a}$. Equation (1) follows.

Note that an atomically periodic (commensurate) minimal superlattice is achieved for those values of $\delta$ and $\theta$ that result in fully integer matrices $\boldsymbol{N} = \mathbb{1} + \boldsymbol{N}'$. The analysis of the elastic properties that follows, however, is a continuum theory that does not rely on precise commensuration and is generally valid as long as $A_0 \gg a_0$.

For later convenience we define here $\vec{G}_0 \equiv 0$, and the momentum "first star," which extends the basis $\vec{G}_{1,2}$ to the six integer combinations thereof that have equal modulus [26,27],

$$\begin{aligned}\vec{G}_0 &= 0,\\ \vec{G}_1 &= -\vec{G}_{-1} = (1,0)\boldsymbol{G},\\ \vec{G}_2 &= -\vec{G}_{-2} = (0,1)\boldsymbol{G},\\ \vec{G}_3 &= -\vec{G}_{-3} = (-1,-1)\boldsymbol{G}.\end{aligned} \tag{3}$$

We make similar definitions for $\vec{g}_j$ and $\vec{g}_j'$, where $j = 0, \pm 1, \pm 2, \pm 3$. A sketch of the reciprocal lattice vectors considered is shown in Fig. 1.

## III. EQUILIBRIUM GRAPHENE DEFORMATION

The moiré superlattice defined in the absence of displacements consists of a smooth spatial variation of the local stacking pattern, which shifts continuously between AA type (local alignment of both carbons in a unit cell to boron and nitrogen), AB type (carbon on boron), and BA type (carbon on nitrogen). Each of these configurations has a different associated adhesion energy density. *Ab initio* calculations [7,28] yield a lower energy for AB stacking, while BA and AA are roughly similar. The difference between $\epsilon_{AB}$, $\epsilon_{BA}$, and $\epsilon_{AA}$ adhesion energies in different regions is denoted by

$$\begin{aligned}\Delta\epsilon_{AB} &= \epsilon_{AB} - \epsilon_{AA},\\ \Delta\epsilon_{BA} &= \epsilon_{BA} - \epsilon_{AA}.\end{aligned}$$

These differences in adhesion create in-plane forces in the two crystals. These forces induce distortions which maximize the area of the favorable AB-stacked regions at the expense of the elastic energy. For a graphene monolayer placed on a thick hBN crystal, it is reasonable to neglect the distortions of hBN. We derive here expressions for the equilibrium graphene displacement field $\vec{u}(\vec{r})$, defined as a minimum of the total energy $U = U_E + U_S$, where $U_E$ is the elastic energy and $U_S$ is the stacking energy (we neglect thermal effects).

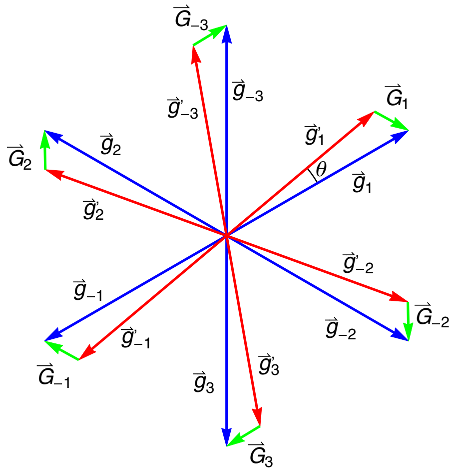

FIG. 1. (Color online) Sketch of the reciprocal lattice vectors $\vec{g}_j'$ of the hBN lattice (red) and of the graphene lattice $\vec{g}_j$ (blue). The green vectors $\vec{G}_j$ describe the moiré superlattice; see text. For clarity, the mismatch between the lattice constants of hBN and graphene has been multiplied by 5.

### A. Elastic energy

The elastic energy $U_E$ per unit cell of a graphene deformation $\vec{u}(\vec{r})$ that is smooth on the atomic spacing is given by continuum elasticity theory,

$$U_E = \frac{1}{N}\int_A \frac{1}{2}[2\mu\,\mathrm{Tr}(\boldsymbol{u}^2) + \lambda\,(\mathrm{Tr}\,\boldsymbol{u})^2]d^2r,$$

where the integral covers a deformation supercell, assumed to be equal to the moiré supercell $\boldsymbol{A}$, which contains $N$ graphene unit cells. Here $\boldsymbol{u} = u_{ij} = \frac{1}{2}(\partial_i u_j + \partial_j u_i)$ is the strain, and $\lambda \approx 3.5$ eV/Å$^2$ and $\mu \approx 7.8$ eV/Å$^2$ are the Lamé factors for graphene. Next, we expand the deformation in harmonics $\vec{u}_{\vec{q}} = \vec{u}^*_{-\vec{q}}$,

$$\vec{u}(\vec{r}) = \sum_{\vec{q}} \vec{u}_{\vec{q}} e^{i\vec{q}\vec{r}}. \tag{4}$$

Note that, if we assume $C_3$-symmetric deformations, the deformation harmonics are related by $2\pi/3$ rotations. Taking this into account, we may write all possible distortions as a combination of four pure classes (see Fig. 2). These are either even or odd respect to a given origin $\vec{r}_0$, depending on whether $\vec{u}(\vec{r}-\vec{r}_0) = \mp\vec{u}(-[\vec{r}-\vec{r}_0])$ (imaginary or real harmonics if $\vec{r}_0 = 0$). They may also be purely longitudinal or purely transverse, depending on whether $\vec{u}_{\vec{q}}$ is parallel or perpendicular to $\vec{q}$. In Sec. IV we will analyze the equilibrium distortions in terms of these components.

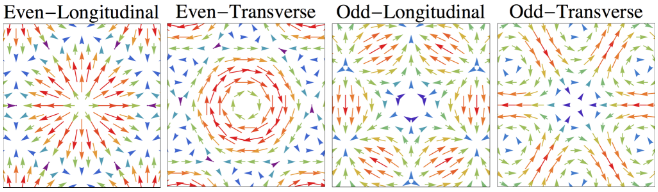

FIG. 2. (Color online) Different types of $C_3$-symmetric distortions, depending on their longitudinal or transverse character and their parity with respect to the origin.

In terms of the $\vec{u}_{\vec{q}}$ harmonics, we may diagonalize $U_E$,

$$U_E = \frac{1}{2}\sum_{\vec{q}} \vec{u}_{-\vec{q}} \boldsymbol{W}_{\vec{q}} \vec{u}_{\vec{q}}. \tag{5}$$

The dynamic matrices $\boldsymbol{W}_{\vec{q}}$ read

$$\boldsymbol{W}_{\vec{q}} = (B \det \boldsymbol{a})\boldsymbol{W}^{\parallel}_{\vec{q}} + (\mu \det \boldsymbol{a})\boldsymbol{W}^{\perp}_{\vec{q}},$$

where $\det \boldsymbol{a}$ is the area of the graphene unit cell, $B = \lambda + 2\mu \approx 21.6\ \text{eV/Å}^2$ is graphene's bulk modulus, and

$$\boldsymbol{W}^{\parallel}_{\vec{q}} = \begin{pmatrix} q_x^2 & q_x q_y \\ q_x q_y & q_y^2 \end{pmatrix}, \quad \boldsymbol{W}^{\perp}_{\vec{q}} = \begin{pmatrix} q_y^2 & -q_x q_y \\ -q_x q_y & q_x^2 \end{pmatrix}. \tag{6}$$

They satisfy $\boldsymbol{W}_{\vec{q}} = \boldsymbol{W}_{-\vec{q}} = \boldsymbol{W}^{\mathrm{T}}_{\vec{q}}$. Note that purely transverse (longitudinal) distortions have only elastic energy contributions from $\mu \boldsymbol{W}^{\perp}_{\vec{q}}$ $(B\boldsymbol{W}^{\parallel}_{\vec{q}})$.

### B. Adhesion potential

We next consider the periodic adhesion potential created by the hBN crystal on the graphene lattice. The simplest model for this potential $V_S(\vec{r})$ (first-star model) is parameterized by $\Delta\epsilon_{AB}$ and $\Delta\epsilon_{BA}$ as defined above and is written, using the definition (3) of the first-star hBN basis $\vec{g}'_j$, as

$$\begin{aligned} V_S(\vec{r}) &= 2\mathrm{Re}\big[v_S\big(e^{i\vec{g}'_1\vec{r}} + e^{i\vec{g}'_2\vec{r}} + e^{i(-\vec{g}'_1-\vec{g}'_2)\vec{r}}\big)\big] + v_0 \\ &= \sum_{j=\pm 1}^{\pm 3} v_j e^{i\vec{g}'_j\vec{r}} + v_0. \end{aligned} \tag{7}$$

Vector $\vec{r}$ in Eq. (7) is the position, in the crystal plane, of the center of any given graphene unit cell, so that $\vec{r} = 0$ corresponds to AA stacking and $\vec{r} = \mp(\vec{a}'_1 + \vec{a}'_2)/3$ corresponds to AB/BA stacking. The complex numbers $v_j$ are defined as

$$v_{j>0} = v^*_{j<0} = v_S = -\frac{\Delta\epsilon_{AB} + \Delta\epsilon_{BA}}{18} + i\frac{\Delta\epsilon_{AB} - \Delta\epsilon_{BA}}{6\sqrt{3}},$$

so that the adhesion potential is a local extremum at these points and their difference is, indeed, $\Delta\epsilon_{AB/BA}$. Note that the constant energy offset in Eq. (7), $v_0 = (\epsilon_{AB} + \epsilon_{BA} + \epsilon_{AA})/3$, is irrelevant for the purpose of computing the equilibrium deformations.

The total adhesion energy per graphene unit cell is the sum, over all $N$ graphene unit cells positions $\vec{R}_{\vec{n}}$ contained in a moiré supercell, of the adhesion potential

$$U_S = \frac{1}{N}\sum_{\vec{n}}^{N} V_S(\vec{R}_{\vec{n}}).$$

The positions $\vec{R}_{\vec{n}}$ above are

$$\vec{R}_{\vec{n}} = \vec{r}_{\vec{n}} + \vec{u}(\vec{r}_{\vec{n}}),$$

where $\vec{r}_{\vec{n}} = \vec{n}\boldsymbol{a}$ are the unstrained unit cells positions and $\vec{n} = (n_1,n_2)$ is a vector of integers. Using the fact that $\boldsymbol{g}\boldsymbol{a} = 2\pi$, we have $e^{i\vec{g}'_j\vec{r}_{\vec{n}}} = e^{i(\vec{g}'_j-\vec{g}_j)\vec{r}_{\vec{n}}} = e^{-i\vec{G}_j\vec{r}_{\vec{n}}}$, so that $U_S$ reads

$$\begin{aligned} U_S &= \frac{1}{\det \boldsymbol{A}}\int_{\boldsymbol{A}} d^2r\, \tilde{V}_S[\vec{r},\vec{u}(\vec{r})], \\ \tilde{V}_S[\vec{r},\vec{u}(\vec{r})] &= \sum_{j=\pm 1}^{\pm 3} v_j e^{-i\vec{G}_j\vec{r}} e^{i\vec{g}'_j\vec{u}(\vec{r})}, \end{aligned} \tag{8}$$

where we have transformed the sum into an integral over the moiré supercell of area $\det \boldsymbol{A}$ since the form of the integrand $\tilde{V}_S[\vec{r},\vec{u}(\vec{r})]$ is now smooth on the atomic scale. This last step transforms our description into a continuum theory on the moiré supercell, for which the AB/BA stacked regions are located at $\vec{r} = \pm(\vec{A}_1 + \vec{A}_2)/3$. Note, however, that the large hBN momenta $\vec{g}'_j$ are retained, associated with the displacements $\vec{u}(\vec{r})$.

To minimize the total energy analytically we need to assume that displacements $\vec{u}$ are small compared to the hBN lattice constant. This is the linear distortion regime and allows us to expand $\tilde{V}_S$ to first order in $\vec{u}(\vec{r})$,

$$\tilde{V}_S[\vec{r},\vec{u}(\vec{r})] \approx \tilde{V}_S[\vec{r},0] + \vec{u}(\vec{r})\partial_{\vec{u}}\tilde{V}_S[\vec{r},\vec{u}(\vec{r})]|_{\vec{u}=0}. \tag{9}$$

Using, once again, a harmonic decomposition for $\vec{u}(\vec{r})$, Eq. (4), we arrive at an adhesion energy that depends only on the harmonics $\vec{u}_{\vec{q}}$ for momenta $\vec{q} = \vec{G}_j$ in the first star of the moiré superlattice,

$$U_S = i\sum_{j=\pm 1}^{\pm 3} v_j \vec{g}'_j \vec{u}_{\vec{G}_j}.$$

This is a generic feature of the linear distortion theory: if the microscopic adhesion profile $V_S(\vec{r})$ is composed of a set of harmonics with momentum $\vec{q}_i = \vec{m}_i\boldsymbol{g}'$ (integer $\vec{m}_i$), the linearized adhesion energy will depend only on distortion harmonics with momentum $\vec{m}_i\boldsymbol{G}$.

The equilibrium values of distortion harmonics $\vec{u}_{\vec{q}}$ are obtained by minimizing $U = U_S + U_E$. Since $U_E$ is quadratic on $\vec{u}_{\vec{q}}$, all harmonics *different* from $\vec{u}_{\vec{G}_j}$ in adhesion energy will be zero in equilibrium. For the remaining six harmonics, we obtain, by differentiating $U$,

$$\vec{u}_{\vec{G}_j} = i v_j^* \boldsymbol{W}^{-1}_{\vec{G}_j}\vec{g}'_j, \tag{10}$$

This is the main analytical result of this section. At $\theta = 0$, $\vec{u}_{\vec{G}_j}$ become $\vec{u}_{\vec{G}_j} = i[(1+\delta)v_j^*/(2\delta^2\pi B a_0^2)]\vec{g}'_j/|\vec{g}'_j|$. We have checked that quadratic terms in the displacements, which arise from expanding the adhesion potential to second order, do not significantly modify this estimate. Moreover, the quadratic expansion confirms that the displacements in Eq. (10) are at least a local minimum of the sum of elastic and adhesion energies.

From Eq. (10) we can compute analytical expressions for a number of observables. In particular, one may compute the strain tensor $\boldsymbol{u}(\vec{r}) = u_{ij}(\vec{r}) = \frac{1}{2}[\partial_i u_j(\vec{r}) + \partial_j u_i(\vec{r})]$ and other important related observables, such as the relative expansion of the lattice at a given point $\frac{1}{2}\mathrm{Tr}\,\boldsymbol{u}$. Evaluating, e.g., the relative lattice expansion at $\theta = 0$, we find a simple expression for the difference between the relative expansion in the center of the AB region and in AA regions:

$$\frac{1}{2}\Sigma_{i=x,y}\left[u_{i,i}^{AB} - u_{i,i}^{AA}\right] = \frac{\epsilon_{\mathrm{AA}} - \epsilon_{\mathrm{AB}}}{\sqrt{3}\delta B a_0^2}. \qquad (11)$$

This quantity has been measured to be greater than 2% [21,29].

### C. Pseudogauge fields

A strain field in graphene is known to produce an effective pseudogauge field due to the modulation of nearest-neighbor-hopping amplitude $t \approx 2.78$ eV with the displacements [30–32] (not to be confused with interlayer pseudogauge fields [33–35]). In terms of the dimensionless parameter $\beta = d\log t/d\log a_0 \approx 2$, the pseudogauge potential is given by

$$\vec{\mathcal{A}}(\vec{r}) = \pm\frac{\beta t}{ev_F}\begin{pmatrix} u_{xx} - u_{yy} \\ -2u_{xy} \end{pmatrix}, \qquad (12)$$

where the strain tensor $\boldsymbol{u}(\vec{r}) = u_{ij}(\vec{r})$ is written in a coordinate frame with the AB bond aligned along the $y$ direction and the $\pm$ sign corresponds to the two valleys (we will focus on the $+$ sector in the following; the opposite one is trivially related by time-reversal symmetry). In the next section we will analyze the effect of this field on the low-energy electronic structure.

If we consider that, according to the solution Eq. (10), only the first-star harmonics of $\vec{u}(\vec{r})$ are nonzero, we obtain a pseudogauge potential that is likewise within the first star, $\vec{\mathcal{A}}(\vec{r}) = \sum_{j=\pm 1}^{\pm 3}\vec{\mathcal{A}}_j e^{i\vec{G}_j\vec{r}}$, where the $\vec{\mathcal{A}}_j = \vec{\mathcal{A}}_{-j}^*$ harmonics can be written, following Eq. (10), as

$$\vec{\mathcal{A}}_j = \frac{\beta t}{ev_F}\begin{pmatrix} i\vec{G}_j\boldsymbol{\sigma}_z\vec{u}_j \\ -i\vec{G}_j\boldsymbol{\sigma}_x\vec{u}_j \end{pmatrix}, \qquad (13)$$

where $\boldsymbol{\sigma}_i$ are Pauli matrices. The associated pseudomagnetic field $\mathcal{B}(\vec{r}) = \partial_x\mathcal{A}_y - \partial_y\mathcal{A}_x = \sum_{j=\pm 1}^{\pm 3}\mathcal{B}_j e^{i\vec{G}_j\vec{r}}$ has harmonics $\mathcal{B}_j = \mathcal{B}_{-j}^* = -\vec{G}_j\boldsymbol{\sigma}_y\vec{\mathcal{A}}_j$.

It is interesting to note that while the typical equilibrium distortions of Eq. (10) scale as $A_0^2$ (since $\boldsymbol{W}_{\vec{G}_j} \sim A_0^{-2}$), the pseudomagnetic field $\mathcal{B}$ contains two spatial derivatives that cancel this scaling, so, unlike $\vec{u}$, it is not expected to vanish as the angle $\theta$ increases. Its effect on the electronic structure, however, will be diminished since the physically relevant ratio of magnetic length to moiré period will increase.

For the case when the hBN and graphene axes are aligned, we can use the estimate for the strain in Eq. (11), and we obtain a typical value for the effective magnetic length $\ell_{\mathcal{B}} = \sqrt{\hbar/|e\mathcal{B}|}$ in terms of the elastic properties of graphene and the adhesion to the substrate,

$$\ell_{\mathcal{B}} = \frac{3}{4\sqrt{\pi}}\sqrt{\frac{\hbar(1+\delta)Ba_0^2}{\beta|\epsilon_{AA} - \epsilon_{AB}|}}a_0. \qquad (14)$$

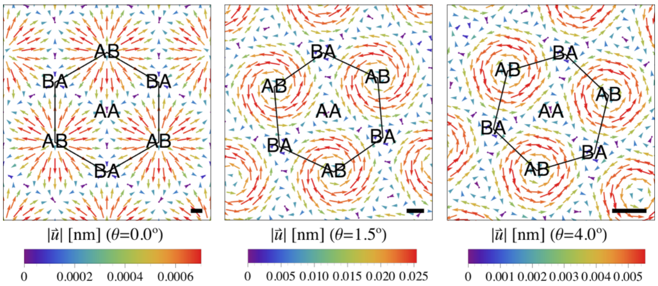

FIG. 3. (Color online) Displacement field $\vec{u}$ (scaled for visibility) in real space for (left) rotation angle $\theta = 0$, (middle) $\theta = 1.5°$, and (right) $\theta = 4°$. Spatial positions are normalized to the moiré period $A_0$. Black scale bars correspond to 1 nm.

## IV. DISCUSSION

The different quantities computed in the preceding section depend critically on the adhesion energy differences $\Delta\epsilon_{AB/BA}$, compared to the typical elastic energy of graphene $\sim a_0^2 B \approx 97$ eV, multiplied by some power of $\delta \approx 1.8\%$ (recall that $\lambda \approx 3.5$ eV/Å$^2$ and $\mu \approx 7.8$ eV/Å$^2$). The adhesion energies have been computed using different *ab initio* and semiempirical approaches [7,13,28,36]. These calculations give values in the range of tens of meV per unit cell for $\Delta\epsilon_{AB}$ and much lower values for $\Delta\epsilon_{BA}$. On the other hand, the experiment of Ref. [21] showed a difference of at least 2% in the local lattice parameter between AB and AA regions. Using Eq. (11), we see that, if the elastic moduli of graphene are not significantly modified by the presence of hBN, the adhesion energy differences should be at least $-60$ meV/unit cell to account for the observed deformation, with Refs. [28,36] suggesting values even greater than $-100$ meV/unit cell when taking into account the London dispersion forces. We use this latter value for $\Delta\epsilon_{AB}$, with $\Delta\epsilon_{BA}$ a tenth of that, which yields results in good agreement with the experiment.

The solution for the strain field of Eq. (10) is plotted in Fig. 3 for rotation angles $\theta = 0°$, $\theta = 1.5°$, and $\theta = 4°$. We see that the magnitude of the displacements is indeed much smaller than the lattice constant $a_0' = 0.251$ nm, which justifies our linear expansion in $\vec{g}_j'\vec{u}(\vec{r})$. We also see that, at $\theta = 0$, the solution approaches a pure longitudinal mode that is even with respect to the AB point (see Fig. 2). This solution is thus dominated by local expansion. As the angle is increased, we see how the solution crosses over to an even-transverse mode with respect to the AB point, which is dominated by local twists and increased shear. The local expansion $\frac{1}{2}\mathrm{Tr}\,\boldsymbol{u}$ associated with these distortions is shown in Fig. 4. The equilibrium strain for the adhesion and elasticity parameters used reaches very large

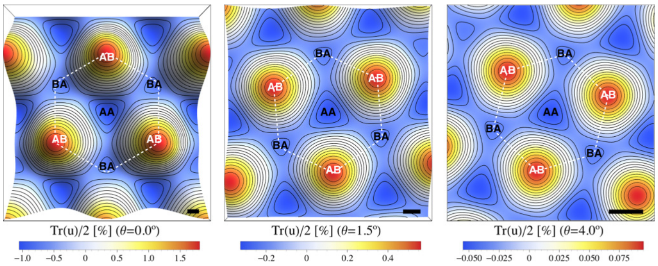

FIG. 4. (Color online) Relative local expansion $\frac{1}{2}\mathrm{Tr}\,\boldsymbol{u}$ in real space for (left) rotation angle $\theta = 0$, (middle) $\theta = 1.5°$, and (right) $\theta = 4°$. Large values of the strain are obtained for $\theta = 0$. Black scale bars correspond to 1 nm.

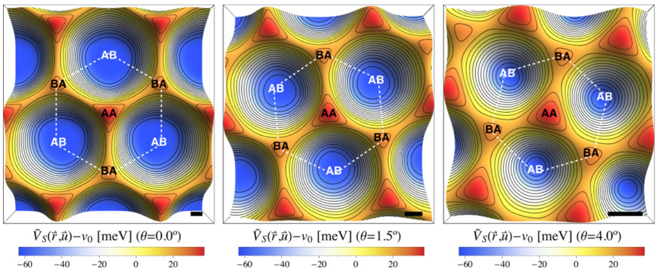

FIG. 5. (Color online) Adhesion energy density $\tilde{V}_S[\vec{r},\vec{u}(\vec{r})]$ in real space, relative to the average adhesion $v_0$, for (left) rotation angle $\theta = 0$, (middle) $\theta = 1.5^\circ$, and (right) $\theta = 4^\circ$. Black scale bars correspond to 1 nm.

values for $\theta = 0$. In the AB region the lattice expands by $da_0$, so that $a_0 + da_0 \approx a_0'$. The relative expansion $da_0/a_0 = \frac{1}{2}\mathrm{Tr}\,\boldsymbol{u}$ reaches its maximum value $\delta = 1.8\%$, which corresponds to adhesion dominating the total energy. In the other regions the lattice is compressed by a comparable, although somewhat smaller, amount, so that the difference surpasses 2%, as found experimentally [21].

The adhesion energy $\tilde{V}_S[\vec{r},\vec{u}(\vec{r})]$ of Eq. (9) is shown in Fig. 5. The uniform blue regions around $\theta = 0$ (left panel) correspond to AB regions in near-perfect registry, where the lattice locally expands by the effect of the adhesion. Surrounding these uniform commensurate regions are sharp hexagonal boundaries, with (different) local maxima at the AA and BA points. It is clear that as the rotation angle $\theta$ increases and the moiré period decreases, the adhesion energy loses to the elastic energy, and the strain field is quickly suppressed. One way to quantify this effect is to analyze the $\theta$ dependence of the full width at half maximum (FWHM) of the adhesion potential as one moves from one AB region to the next. This is plotted in Fig. 6. A purely unstrained bilayer has a FWHM of $A_0/2$. We can see how this value decreases as $A_0$ is increased.

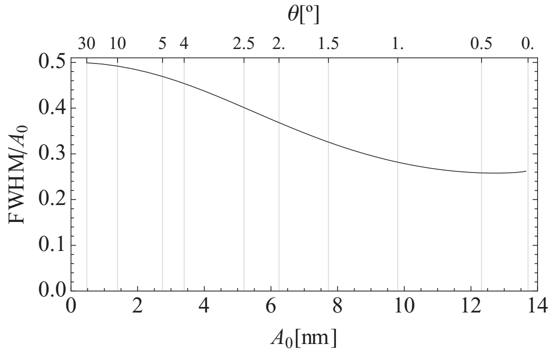

FIG. 6. Normalized FWHM of the hexagonal boundaries in the adhesion energy density (see Fig. 5, left) as a function of rotation angle $\theta$ or moiré period $A_0$.

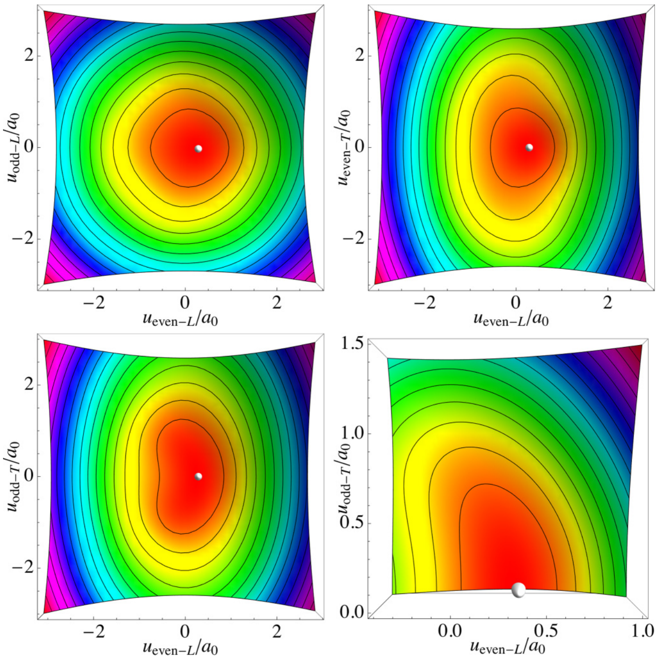

FIG. 7. (Color online) Total energy (elastic plus adhesion) at $\theta = 0$ beyond the linear approximation [using Eqs. (5) and (8)] as a function of pure distortion amplitudes $u_{\mathrm{even/odd-L/T}}$ (see Fig. 2). Note that the minimum (white dot), given by Eq. (10), is absolute and is not destabilized by nonlinear corrections.

The spatial patterns of the vertical Young's modulus recently measured with AFM by Woods *et al.* [21] are strongly reminiscent of the adhesion potential profiles shown in Fig. 5, including the small difference between AA and BA vertices along the hexagonal boundary (which are due to the finite $\Delta\epsilon_{BA} < 0$). It can be argued that the measured elastic modulus should indeed reflect, to a certain extent, the spatial modulation of the adhesion potential since a stronger adhesion should correlate to a stiffer elastic modulus with respect to vertical deformations. The FWHM of the experimental elastic modulus also shows a strong decrease as the angle approaches zero. However, the way this decrease happens is far more abrupt in the experiment than in our model, apparently dropping discontinuously at around $A_0 \approx 10$ nm ($\theta = 1^\circ$). This suggests effects beyond our present model, such as the possibility of an additional contribution to the total energy, the formation of ripples whereby the interlayer distance acquires a spatial texture, or even a global commensurate-incommensurate transition that is associated with a sudden jump in the area of the graphene sample as the angle is decreased [37]. These considerations remain beyond the scope of this work and require numerical computation of a rather different kind. We have evaluated within our analytical framework the effect of including additional harmonics in the adhesion potential in Eq. (7), such as those described in Ref. [13], but the results of Fig. 6 do not change qualitatively. We have likewise excluded the possibility of first- and second-order phase transitions as a result of nonlinear terms in Eq. (9). This is clear from the profile of the total energy $U = U_S + U_E$ around $\theta = 0$, computed using the unexpanded adhesion $U_S$ of Eq. (8). $U$ is shown in Fig. 7 as a function of longitudinal/transverse and even/odd distortion amplitudes, $u_{\mathrm{even/odd-L/T}}$. Note that the potential minimum in Eq. (10) (white dot in Fig. 7) remains stable and is the true absolute minimum of the potential. This remains valid even in the unrealistic extreme of vanishing shear modulus (not shown).

Finally, the pseudomagnetic field associated with the strain is shown in Fig. 8. The large strains involved in the equilibrium

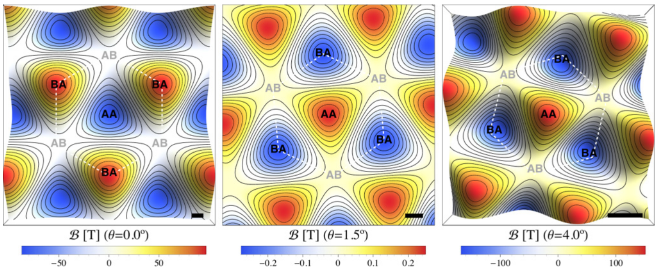

FIG. 8. (Color online) Pseudomagnetic field $\mathcal{B}(\vec{r})$ in real space for (left) rotation angle $\theta = 0$, (middle) $\theta = 1.5^\circ$, and (right) $\theta = 4^\circ$. Large fields above 200 T are produced by the strains. Black scale bars correspond to 1 nm.

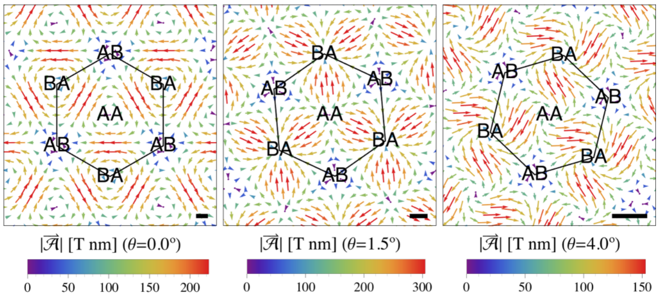

FIG. 10. (Color online) Pseudogauge potential $\vec{\mathcal{A}}(\vec{r})$ in real space for (left) rotation angle $\theta = 0$, (middle) $\theta = 1.5^\circ$, and (right) $\theta = 4^\circ$. Note the vorticity inversion at $\theta = \theta_{\mathcal{B}} = 1.5^\circ$. Black scale bars correspond to 1 nm.

configuration produce very large pseudomagnetic fields up to 200 T. Surprisingly, however, the spatial pattern experiences an inversion at a finite but small angle $\theta_{\mathcal{B}}$, around which the pseudomagnetic field is suppressed and changes sign. The range of spatial variation of $\mathcal{B}$ as a function of $\theta$ is shown in Fig. 9, which reveals the inversion at $\theta_{\mathcal{B}} \approx 1.5^\circ$. Analyzing the vector potential $\vec{\mathcal{A}}(\vec{r})$ at this particular rotation angle, we find a similar pattern as that in Fig. 3 (left panel): while $\vec{\mathcal{A}}(\vec{r})$ is nonzero, it has a vanishing curl, so it is a pure gauge (purely longitudinal field, odd with respect to AB; see Fig. 2). Its vorticity, in fact, becomes inverted at this $\theta_{\mathcal{B}}$. This is shown in Fig. 10. Apart from the field inversion, the typical magnitude of the pseudomagnetic field is roughly in the range 100–200 T throughout all angles, although its physical effects on the electronic structure should be stronger at small angles, where the magnetic length is much smaller than the moiré period.

## V. SPECTRAL GAP

The problem of assessing the spectral gap of graphene coupled to the gapped hBN crystal can be analyzed assuming that the hBN gap ($\Delta_{\rm hBN} \approx 5.2$ eV) is much larger than the energy scales under consideration. In this limit, its effect on graphene's low-energy effective Dirac Hamiltonian is the addition of a position-dependent SU(2) self-energy $\boldsymbol{\Sigma}(\vec{r})$ [14,38,39]. Its absolute magnitude is $m_0 = t_\perp^2/(\Delta_{\rm hBN}/2) \approx 35$ meV, where $t_\perp \sim 0.3$ eV is the graphene-hBN hopping amplitude. The gap at the Dirac point can be approximated to first order in $m_0$ as the spatial average of the local gap $\mathrm{Tr}[\boldsymbol{\sigma}_z\boldsymbol{\Sigma}(\vec{r})]$ in a supercell $\boldsymbol{A}$ of area $\det\boldsymbol{A}$:

$$\Delta^{(1)}_{\rm eff} = \frac{1}{\det\boldsymbol{A}}\int_{\boldsymbol{A}} d^2r\,\mathrm{Tr}[\boldsymbol{\sigma}_z\boldsymbol{\Sigma}(\vec{r})] + O\left(m_0^2\right). \qquad (15)$$

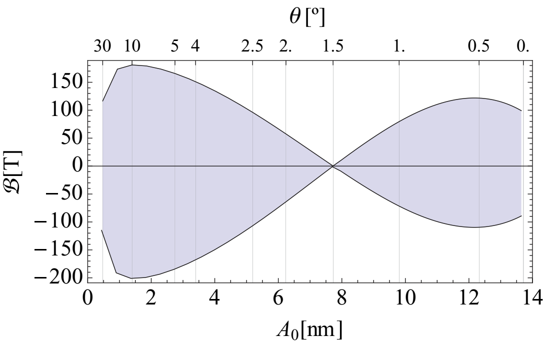

FIG. 9. (Color online) Range of variation of magnetic field $\mathcal{B}$ throughout the sample as a function of rotation angle $\theta$ or moiré period $A_0$. Note the large ∼200 T maximum fields, even for large angles, and the zero at $\theta_{\mathcal{B}} \approx 1.5^\circ$.

In the absence of strains, it can be shown that the local gap $\Delta^{(1)}_{\rm eff}(\vec{r}) = \mathrm{Tr}[\boldsymbol{\sigma}_z\boldsymbol{\Sigma}^{(0)}(\vec{r})]$ [where $\boldsymbol{\Sigma}^{(0)}(\vec{r}) = \boldsymbol{\Sigma}(\vec{r})|_{\vec{u}=0}$] has a zero spatial average. The AB and BA regions will have a positive local gap $\Delta^{(1)}_{\rm eff}(\vec{r}_{\rm AB}) = \Delta^{(1)}_{\rm eff}(\vec{r}_{\rm BA}) = m_0$, while the AA region will have a negative local gap that, without strains, exactly cancels the former, $\Delta^{(1)}_{\rm eff}(\vec{r}_{\rm AA}) = -2m_0$, so that the averaged gap $\Delta^{(1)}_{\rm eff}$ is zero.

The effect of spontaneous strains, as we saw, is to expand the AB regions at the expense of BA and AA. This breaks the cancellation of the average $\Delta^{(1)}_{\rm eff}(\vec{r})$, and hence, strains will create an integrated gap $\Delta^{(1)}_{\rm eff} \neq 0$ at the Dirac point [38]. In the extreme case where the effective AB-stacked area grows from $A/3$ to cover most of the supercell area $A$, the average gap will become $m_0 \approx 35$ meV. In the more realistic case described here, the linear size of the AB region at $\theta = 0$ is around 70%–75% of the supercell diameter, which yields an estimate for the gap of around 15 meV. A figure closer to the maximum $m_0$ would be obtained for stronger adhesion parameters, which would result in a larger AB region (smaller FWHM in Fig. 6).

Interestingly, it has been noted [40] that in the presence of strains, there is another contribution beyond Eq. (15) that further increases the effective gap by around 40% [actually $\beta/(\sqrt{3}\pi)$, to be precise]. This comes about in the second order of perturbation theory in the pseudogauge field $\vec{\mathcal{A}}(\vec{r})$ and the scalar potential $\boldsymbol{\sigma}_0\boldsymbol{\Sigma}^{(0)}(\vec{r})$. Specifically, the gap is corrected by

$$\Delta^{(2)}_{\rm eff} = -\sum_{s,s'=\pm}\sum_{\vec{k}} \frac{\langle\psi_0^{s'}|v_F e\vec{\mathcal{A}}(\vec{r})\vec{\boldsymbol{\sigma}}|\psi_{\vec{k}}^{s}\rangle\langle\psi_{\vec{k}}^{s}|\boldsymbol{\sigma}_0\boldsymbol{\Sigma}^{(0)}(\vec{r})|\psi_0^{s'}\rangle}{E_0 - E_{\vec{k}}^{s}} + \text{c.c.} \qquad (16)$$

(see Ref. [38] for higher-order corrections). In the expression above, $E^{\pm}_{\vec{k}} = \pm v_F|\vec{k}|$ are conduction and valence eigenenergies of the unperturbed Dirac Hamiltonian (Dirac point at the origin $E_0 = 0$), and $|\psi^s_{\vec{k}}\rangle$ are the corresponding plane-wave eigenstates, with pseudospin $(1,(k_x + isk_y)/|\vec{k}|)/\sqrt{2}$. The sum

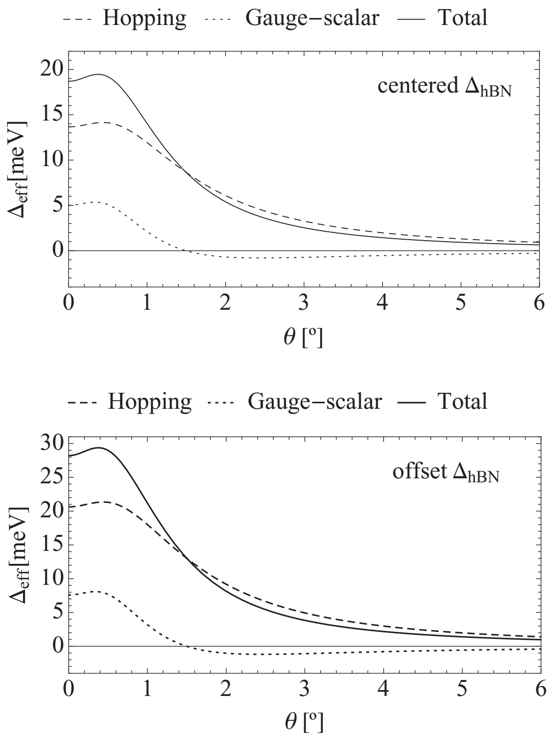

FIG. 11. Effective spectral gap induced by hBN on graphene under equilibrium strains as a function of relative angle $\theta$. We assume (top) an hBN gap centered around graphene's neutrality point and (bottom) a 1.3 eV offset between the two and decompose the gap into its two leading contributions (dashed and dotted lines).

over $\vec{k}$ in Eq. (16) is constrained to the first-star momenta of Eq. (3), which are the harmonics of $\vec{\mathcal{A}}(\vec{r})$ [see Eq. (13)]. For all of these momenta, the denominator is $E_0 - E^{\pm}_{\vec{k}} = \pm v_F|\vec{G}|$. Combining this with the solution in Eqs. (13) and (10) and the corresponding form of the unperturbed $\boldsymbol{\sigma}_0\boldsymbol{\Sigma}^{(0)}(\vec{r})$ [38,39], we can obtain closed expressions for $\Delta^{(1)}_{\rm eff}$ and $\Delta^{(2)}_{\rm eff}$. Interestingly, both contributions are parametrically equal in a systematic expansion in the deformations $\vec{u}$ and the inverse hBN gap $\Delta^{-1}_{\rm hBN}$. Specifically, $\Delta^{(2)}_{\rm eff} = \frac{\beta}{\sqrt{3\pi}}\Delta^{(1)}_{\rm eff}$. For $\theta = 0$ the total gap reads

$$\Delta_{\rm eff} = \Delta^{(1)}_{\rm eff} + \Delta^{(2)}_{\rm eff} = -\frac{2}{9\sqrt{3}}\frac{1+\delta}{\delta^2}\left(1+\frac{\beta}{\sqrt{3\pi}}\right) \times \frac{m_+(\Delta\epsilon_{AB}+\Delta\epsilon_{BA}) + m_-(\Delta\epsilon_{AB}-\Delta\epsilon_{BA})}{Ba_0^2}. \tag{17}$$

The chosen sign corresponds to the $K$ valley and is inverted in the $K'$ valley. The masses $m_\pm = \frac{t_\perp^2}{2}(\epsilon_c^{-1} \pm \epsilon_v^{-1})$ are defined in terms of the conduction- and valence-band edges $\epsilon_{c,v}$ in hBN with respect to graphene's neutrality point (if the gap is centered, $m_- = m_0$ and $m_+ = 0$). Recall also that $\delta \approx 1.8\%$, $\beta \approx 2$, and that the bulk modulus of graphene is $B \approx 19.1$ meV/Å$^2$. With our assumption for the adhesion energies, the gap at $\theta = 0$ is approximately $\Delta_{\rm eff} \approx 20$ meV. This value for $\Delta_{\rm eff}$ is in qualitative agreement with experimental observations [22]. The effective gap $\Delta_{\rm eff}$ as a function of $\theta$ is shown in Fig. 11. Note that the gauge-scalar contribution vanishes, as expected, at the special $\theta_B \sim 1.5°$ angle, for which the pseudomagnetic field vanishes. Note that a finite-energy offset between the Dirac point and the gap center of hBN ($m_+ \neq 0$) can result in a further increase of the induced gap. As an example, a shift of ~1.3 eV between the two yields a $\theta = 0$ value of $\Delta_{\rm eff} \approx 30$ meV (see Fig. 11, bottom panel), in quantitative agreement with experiment.

## VI. CONCLUSIONS

We have presented a model for the in-plane deformations of a graphene layer on an hBN substrate. The deformations, effective magnetic field, and average gap can be expressed in terms of the elastic properties of graphene, the lattice mismatch, and the adhesion energy between graphene and hBN [see Eqs. (11), (14), and (17)]. The estimates presented here give an electronic gap of a few tens of meV, in line with experiments. The average strains near perfect alignment are a few percent, $\sim\delta$, and give rise to effective pseudomagnetic fields of the order of 50–100 T. The pseudomagnetic length is a few nanometers, about one order of magnitude smaller than the dimensions of the superlattice unit cell, which should therefore lead to strong effects in the electronic structure.

The different components of the potential induced by the moiré superlattice include even and odd terms under spatial inversion of similar magnitude, as expected from an hBN substrate. The combination of a modulated scalar and a gauge potential gives a contribution to the average gap which has the same parametric dependence and order of magnitude as the gap arising from the enlargement of the energetically favorable $AB$ regions.

The main results arise from a competition between the rigidity of the graphene layer and the adhesion potential provided by the substrate. For realistic parameters, the graphene deformations are small, and pinning and commensuration effects are not important. In terms of an effective Frenkel-Kontorova model [37], the results presented here are consistent with a floating phase with gapless acoustic modes.

## ACKNOWLEDGMENTS

We thank K. S. Novoselov, A. K. Geim, A. Cortijo, and F. Barbero for useful discussions. We acknowledge support from the Spanish Ministry of Economy (MINECO) through Grants No. FIS2011-23713 and No. PIB2010BZ-00512, the European Research Council Advanced Grant (Contract No. 290846), and the European Commission under the Graphene Flagship, Contract No. CNECT-ICT-604391.

---

[1] L. A. Ponomarenko, A. K. Geim, A. A. Zhukov, R. Jalil, S. V. Morozov, K. S. Novoselov, I. V. Grigorieva, E. H. Hill, V. V. Cheianov, V. I. Fal'ko, K. Watanabe, T. Taniguchi, and R. V. Gorbachev, Nat. Phys. **7**, 958 (2011).

[2] J. Xue, J. Sanchez-Yamagishi, D. Bulmash, P. Jacquod, A. Deshpande, K. Watanabe, T. Taniguchi, P. Jarillo-Herrero, and B. J. LeRoy, Nat. Mater. **10**, 282 (2011).

[3] C. Dean, A. Young, I. Meric, C. Lee, L. Wang, S. Sorgenfrei, K. Watanabe, T. Taniguchi, P. Kim, K. Shepard *et al.*, Nat. Nanotechnol. **5**, 722 (2010).

[4] M. Yankowitz, J. Xue, and B. J. LeRoy, J. Phys. Condens. Matter **26**, 303201 (2014).

[5] A. V. Kretinin, Y. Cao, J. S. Tu, G. L. Yu, R. Jalil, K. S. Novoselov, S. J. Haigh, A. Gholinia, A. Mishchenko, M. Lozada, T. Georgiou, C. Woods, F. Withers, P. Blake, G. Eda, A. Wirsig, C. Hucho, K. Watanabe, T. Taniguchi, A. K. Geim, and R. V. Gorbachev, Nano Lett. **14**, 3270 (2014).

[6] J. Slawinska, I. Zasada, and Z. Klusek, Phys. Rev. B **81**, 155433 (2010).

[7] B. Sachs, T. O. Wehling, M. I. Katsnelson, and A. I. Lichtenstein, Phys. Rev. B **84**, 195414 (2011).

[8] M. Kindermann, B. Uchoa, and D. L. Miller, Phys. Rev. B **86**, 115415 (2012).

[9] D. S. L. Abergel, J. R. Wallbank, X. Chen, M. Mucha-Kruczynski, and V. I. Fal'ko, New J. Phys. **15**, 123009 (2013).

[10] M. Mucha-Kruczynski, J. Wallbank, and V. Fal'ko, Phys. Rev. B **88**, 205418 (2013).

[11] M. Diez, J. P. Dahlhaus, M. Wimmer, and C. W. J. Beenakker, Phys. Rev. Lett. **112**, 196602 (2014).

[12] J. C. W. Song, P. Samutpraphoot, and L. S. Levitov, arXiv:1404.4019.

[13] M. Neek-Amal and F. M. Peeters, Appl. Phys. Lett. **104**, 041909 (2014).

[14] J. Jung, A. DaSilva, S. Adam, and A. H. MacDonald, arXiv:1403.0496.

[15] X. Chen, J. R. Wallbank, A. A. Patel, M. Mucha-Kruczynski, E. McCann, and V. I. Fal'ko, Phys. Rev. B **89**, 075401 (2014).

[16] M. Bokdam, T. Amlaki, G. Brocks, and P. J. Kelly, Phys. Rev. B **89**, 201404(R) (2014).

[17] L. A. Ponomarenko, R. V. Gorbachev, G. L. Yu, D. C. Elias, R. Jalil, A. A. Patel, A. Mishchenko, A. S. Mayorov, C. R. Woods, J. R. Wallbank, M. Mucha-Kruczynski, B. A. Piot, M. Potemski, I. V. Grigorieva, K. S. Novoselov, F. Guinea, V. I. Fal'ko, and A. K. Geim, Nature (London) **497**, 594 (2013).

[18] S. Tang, H. Wang, Y. Zhang, A. Li, H. Xie, X. Liu, L. Liu, T. Li, F. Huang, X. Xie, and M. Jiang, Sci. Rep. **3**, 2666 (2013).

[19] M. Yankowitz, J. Xue, D. Cormode, J. D. Sanchez-Yamagishi, K. Watanabe, T. Taniguchi, P. Jarillo-Herrero, P. Jacquod, and B. J. LeRoy, Nat. Phys. **8**, 382 (2012).

[20] G. L. Yu, R. V. Gorbachev, J. S. Tu, A. V. Kretinin, Y. Cao, R. Jalil, F. Withers, L. A. Ponomarenko, B. A. Piot, M. Potemski, D. C. Elias, X. Chen, K. Watanabe, T. Taniguchi, I. V. Grigorieva, K. S. Novoselov, V. I. Fal'ko, A. K. Geim, and A. Mishchenko, Nat. Phys. **10**, 525 (2014).

[21] C. R. Woods, L. Britnell, A. Eckmann, G. L. Yu, R. V. Gorbachev, A. Kretinin, J. Park, L. A. Ponomarenko, M. I. Katsnelson, Y. N. Gornostyrev, K. Watanabe, T. Taniguchi, C. Casiraghi, A. K. Geim, and K. S. Novoselov, Nat. Phys. **10**, 451 (2014).

[22] B. Hunt, J. D. Sanchez-Yamagishi, A. F. Young, M. Yankowitz, B. J. LeRoy, K. Watanabe, T. Taniguchi, P. Moon, M. Koshino, P. Jarillo-Herrero, and R. C. Ashoori, Science **340**, 1427 (2013).

[23] F. Amet, J. R. Williams, K. Watanabe, T. Taniguchi, and D. Goldhaber-Gordon, Phys. Rev. Lett. **110**, 216601 (2013).

[24] M. Neek-Amal and F. M. Peeters, Appl. Phys. Lett. **104**, 173106 (2014).

[25] The moiré pattern is a spatial beating pattern, hence the definition of $\boldsymbol{G}$ as the difference of the two spatial frequencies $\boldsymbol{g}$ and $\boldsymbol{g}'$. As in beating waves, this does not necessarily imply periodicity (commensuration) at the atomic level, i.e., at the level of the "carrier waves" of frequency $\boldsymbol{g} + \boldsymbol{g}'$.

[26] S. Shallcross, S. Sharma, E. Kandelaki, and O. A. Pankratov, Phys. Rev. B **81**, 165105 (2010).

[27] M. Kindermann and P. N. First, Phys. Rev. B **83**, 045425 (2011).

[28] V. Caciuc, N. Atodiresei, M. Callsen, P. Lazić, and S. Blügel, J. Phys. Condens. Matter **24**, 424214 (2012).

[29] M. Yankowitz and B. J. LeRoy (private communication).

[30] H. Suzuura and T. Ando, Phys. Rev. B **65**, 235412 (2002).

[31] F. Guinea, B. Horovitz, and P. Le Doussal, Phys. Rev. B **77**, 205421 (2008).

[32] A. H. C. Neto, F. Guinea, N. M. R. Peres, K. S. Novoselov, and A. K. Geim, Rev. Mod. Phys. **81**, 109 (2009).

[33] A. A. Pacheco Sanjuan, Z. Wang, H. Pour Imani, M. Vanević, and S. Barraza-Lopez, Phys. Rev. B **89**, 121403(R) (2014).

[34] P. San-Jose, J. González, and F. Guinea, Phys. Rev. Lett. **108**, 216802 (2012).

[35] E. Mariani, A. J. Pearce, and F. von Oppen, Phys. Rev. B **86**, 165448 (2012).

[36] K. Berland and P. Hyldgaard, Phys. Rev. B **87**, 205421 (2013).

[37] P. M. Chaikin and T. C. Lubensky, *Principles of Condensed Matter Physics* (Cambridge University Press, Cambridge, 2000), Vol. 1.

[38] P. San-Jose, Á. Gutiérrez, M. Sturla, and F. Guinea, arXiv:1406.5999.

[39] P. Moon and M. Koshino, arXiv:1406.0668.

[40] T. Low, F. Guinea, and M. I. Katsnelson, Phys. Rev. B **83**, 195436 (2011).